



Cite this: *Chem. Sci.*, 2018, **9**, 5197

Enhancement of CO₂ binding and mechanical properties upon diamine functionalization of M₂(dobpdc) metal-organic frameworks†

Jung-Hoon Lee, ^{ab} Rebecca L. Siegelman, ^{cd} Lorenzo Maserati, ^a Tonatiuh Rangel, ^{ab} Brett A. Helms, ^{ad} Jeffrey R. Long, ^{cde} and Jeffrey B. Neaton*^{abf}

The family of diamine-appended metal-organic frameworks exemplified by compounds of the type mmn-M₂(dobpdc) (mmn = *N,N'*-dimethylethylenediamine; M = Mg, Mn, Fe, Co, Zn; dobpdc⁴⁻ = 4,4'-dioxidobiphenyl-3,3'-dicarboxylate) are adsorbents with significant potential for carbon capture, due to their high working capacities and strong selectivity for CO₂ that stem from a cooperative adsorption mechanism. Herein, we use first-principles density functional theory (DFT) calculations to quantitatively investigate the role of mmn ligands in dictating the framework properties. Our van der Waals-corrected DFT calculations indicate that electrostatic interactions between ammonium carbamate units significantly enhance the CO₂ binding strength relative to the unfunctionalized frameworks. Additionally, our computed energetics show that mmn-M₂(dobpdc) materials can selectively adsorb CO₂ under humid conditions, in agreement with experimental observations. The calculations further predict an increase of 112% and 124% in the orientationally-averaged Young's modulus *E* and shear modulus *G*, respectively, for mmn-Zn₂(dobpdc) compared to Zn₂(dobpdc), revealing a dramatic enhancement of mechanical properties associated with diamine functionalization. Taken together, our calculations demonstrate how functionalization with mmn ligands can enhance framework gas adsorption and mechanical properties.

Received 8th December 2017
Accepted 15th May 2018

DOI: 10.1039/c7sc05217k
rsc.li/chemical-science

1 Introduction

Metal-organic frameworks (MOFs) consist of metal clusters or ions that are joined by organic linkers to form porous network solids with large surface areas, high crystallinity, and, in some cases, redox-active open metal sites.^{1–10} MOFs are promising for gas storage and separation applications, particularly in the area of carbon capture,^{11–16} and accordingly have received significant recent attention in the literature. Carbon dioxide is mainly produced from the combustion of fossil fuels, and in 2011 alone such CO₂ emissions exceeded 32 Gt.¹⁶ It is well-known that CO₂ produced by combustion is a major driver of global warming,^{17,18} contributing to rising sea levels and ocean climate

change. Therefore, reducing CO₂ emissions is among the most urgent problems facing humanity today.

Among numerous MOFs currently under investigation for CO₂ capture, frameworks of the type M₂(dobdc) (M = Mg, Mn, Fe, Co, Ni, Cu, Zn; dobdc⁴⁻ = 2,5-dioxidobenzene-1,4-dicarboxylate) have been extensively studied due to their high density of open metal sites, which have been shown to engender high selectivity in the separation of various gas molecules.^{11,19–28} Previous studies have reported impressive uptake capacities, together with heats of CO₂ adsorption at the open metal sites as high as 43.5 kJ mol⁻¹ in Mg₂(dobdc).²⁹ Notably, this value can be tuned by metal substitution,²⁸ although the M₂(dobdc) family exhibits poor CO₂ selectivity in the presence of H₂O.^{30–34} Recently, Mason *et al.*³² reported equilibrium adsorption isotherms for mixtures of CO₂, N₂, and H₂O, the three most prevalent components of flue gas,³⁵ and showed that the CO₂ capture performance of M₂(dobdc) (M = Mg, Ni) is significantly diminished under humid conditions, due to preferential binding of H₂O over CO₂ at the open metal sites. For Ni₂(dobdc), CO₂ uptake is almost zero in the presence of water.

Although the M₂(dobdc) materials do not selectively adsorb CO₂ under humid conditions, functionalization of open metal sites in the expanded framework M₂(dobpdc) (dobpdc⁴⁻ = 4,4'-dioxidobiphenyl-3,3'-dicarboxylate) with *N,N'*-dimethylethylenediamine (mmn) has been shown to enhance both the CO₂

^aMolecular Foundry, Lawrence Berkeley National Laboratory, Berkeley, California 94720, USA. E-mail: jbneaton@lbl.gov

^bDepartment of Physics, University of California, Berkeley, California 94720, USA

^cDepartment of Chemistry, University of California, Berkeley, California 94720, USA

^dMaterials Sciences Division, Lawrence Berkeley National Laboratory, Berkeley, California 94720, USA

^eDepartment of Chemical and Biomolecular Engineering, University of California, Berkeley, California 94720, USA

^fKavli Energy Nanoscience Institute at Berkeley, Berkeley, California 94720, USA

† Electronic supplementary information (ESI) available. See DOI: [10.1039/c7sc05217k](https://doi.org/10.1039/c7sc05217k)

affinity and selectivity under humid conditions.^{36–38} In mmn-M₂(dobpdc), diamine molecules are grafted onto the open metal sites and dangle into the pore interiors. Notably, the measured heat of CO₂ adsorption in mmn-Mg₂(dobpdc) is as high as 71 kJ mol⁻¹, almost 30 kJ mol⁻¹ greater than in Mg(dobdc), and mmn-Mg₂(dobpdc) is also stable under humid conditions.³² The impressive CO₂ capture performance of mmn-Mg₂(dobpdc) and other mmn-M₂(dobpdc) frameworks stems from a unique cooperative CO₂ capture mechanism, which has been shown to persist even in the presence of H₂O, based on infrared spectroscopy measurements.³² Interestingly, multicomponent adsorption measurements additionally show that the amount of adsorbed CO₂ from a mixture of CO₂, N₂, and H₂O in mmn-Mg₂(dobpdc) is slightly higher than that from pure CO₂ in mmn-Mg₂(dobpdc).

In view of its exceptional CO₂ capture performance, we seek to understand quantitatively the properties of mmn-M₂(dobpdc) using accurate first-principle density function theory (DFT) calculations. DFT is the most promising method for studying the adsorption (and related) properties of MOFs at the molecular level, owing to its efficiency and accuracy relative to other quantum mechanical methods. In previous theoretical studies, van der Waals (vdW)-corrected DFT in particular has been shown to accurately predict the binding energies and mechanisms of small gas molecules in MOFs,^{28,29,31,39–42} including MOFs having localized metal 3d electrons and non-zero spin moments.^{43,44} Other properties, such as mechanical strength, can be predicted with similar accuracy.⁴⁵ For mmn-M₂(dobpdc), the CO₂ adsorption mechanism and CO₂ interactions with open metal sites in the form of carbamate have also been successfully studied with DFT methods.^{37,38,46,47}

Prior DFT-based studies notwithstanding,^{37,38,41,46–51} a complete and detailed understanding of the CO₂ adsorption energetics in mmn-M₂(dobpdc) is still lacking. In particular, the contributions of vdW dispersion interactions to adsorption enthalpies and related properties of mmn-M₂(dobpdc) have yet to be quantified, and thus a predictive approach for adsorption energies in these complex systems does not yet exist. Moreover, the strength of electrostatic interactions between the ammonium carbamate units formed upon CO₂ adsorption and the effect of such interactions on key macroscopic observables, such as mechanical properties, have yet to be quantified and understood. Here, we use vdW-corrected DFT calculations to demonstrate a quantitative approach to predict binding and formation energies in this important class of MOFs. We further quantify the significant electrostatic interactions between ammonium carbamate units; compute and understand the effect of adsorption on mechanical properties; and determine the binding site of H₂O on the ammonium carbamate chains and evaluate the influence of humidity on the overall CO₂ performance.

2 Methodology

2.1 Computational details

In order to elucidate the role of mmn ligands in the CO₂ capture properties of mmn-M₂(dobpdc), we perform first-principles DFT calculations within the generalized gradient

approximation (GGA) of Perdew, Burke, and Ernzerhof (PBE).⁵² We use a plane-wave basis and projector augmented-wave (PAW)^{53,54} pseudopotentials with the Vienna *ab initio* Simulation Package (VASP) code.^{55–58} To include the effect of the vdW dispersive interactions on binding energies and mechanical properties, we perform structural relaxations with vdW dispersion-corrected functionals (vdW-DF2)⁵⁹ as implemented in VASP. The initial structures for the MOFs we consider here are obtained from previous studies.^{37,38,51,60} For all calculations, we use (i) a Γ -point sampling of the Brillouin zone and (ii) a 600 eV plane-wave cutoff energy. We explicitly treat two valence electrons for Mg (3s²), seven for Mn (3d⁵4s²), eight for Fe (3d⁶4s²), nine for Co (3d⁷4s²), twelve for Zn (3d¹⁰4s²), six for O (2s²2p⁴), five for N (2s²2p³), four for C (2s²2p²), and one for H (1s¹). All structural relaxations are performed with a Gaussian smearing of 0.05 eV⁶¹ and with the structure constrained to the space group $P3_221$. The computed CO₂ binding energies are within 0.4 kJ mol⁻¹ when we relax these symmetry constraints. The ions are relaxed until the Hellmann–Feynman forces are less than 0.02 eV Å⁻¹. The convergence threshold for self-consistency is 10⁻⁵ eV. For phonon frequency calculations, we use a more rigorous criterion (10⁻⁸ eV) (see Table S4†). Hubbard *U* values of 5.5 eV, 6.5 eV, and 5.3 eV for Mn, Fe, and Co 3d states are chosen following previous studies for M₂(dobdc) (M = Ti, V, Cr, Mn, Fe, Co, Ni, Cu).⁴⁴ Based on the ground state magnetic structure of Fe₂(dobdc),^{21,62} we use ferromagnetic ordering along the metal oxide chain direction and antiferromagnetic ordering between the chains for mmn-M₂(dobpdc) (M = Mn, Fe, Co). Our computed electronic structure and measured adsorption spectra are given in the ESI.†

To compute CO₂ binding energies, we optimize mmn-M₂(dobpdc) prior to CO₂ adsorption ($E_{\text{mmn-MOF}}$), interacting with CO₂ in the gas phase (E_{CO_2}) within a 15 Å × 15 Å × 15 Å cubic supercell, and mmn-M₂(dobpdc) with adsorbed CO₂ molecules ($E_{\text{CO}_2-\text{mmn-MOF}}$) using vdW-corrected DFT. The binding energies (E_B) are obtained *via* the difference

$$-E_B = E_{\text{CO}_2-\text{mmn-MOF}} - (E_{\text{mmn-MOF}} + E_{\text{CO}_2}). \quad (1)$$

We also consider zero-point energy (ZPE) and thermal energy (TE) corrections to compare computed binding energies with experimentally determined CO₂ heats of adsorption, following a previous DFT study.²⁸ We calculate vibrational frequencies of bound CO₂, H₂O, N₂, mmn, and CO₂-mmn in the framework; we also compute vibrational frequencies of free CO₂, H₂O, N₂, mmn, and CO₂-mmn molecules within a 15 Å × 15 Å × 15 Å cubic supercell. In the former case, we assume that changes in the frequency of framework phonon modes are small relative to those of molecular modes. All ZPE and TE corrections are computed at 298 K. All computed Kohn–Sham energies, vibrational frequencies, ZPE, and TE corrections are given in Tables S2, S3, S5, and S6 in the ESI.†

To calculate mechanical properties, we generate the stress tensor with (i) the Γ -point, (ii) a 1000 eV plane-wave cutoff energy, and (iii) a 0.01 eV Å⁻¹ force criterion. The linear elastic properties are then obtained using Hooke's law, which describes the relationship between stress, σ , and strain, ε :



$$\sigma_i = C_{ij}\varepsilon_j \quad (2)$$

where the C_{ij} are components of the single crystal elastic stiffness tensor. Here, we adopt the standard Voigt notation, with C_{ij} calculated as follows.⁶³ First, we fully relax the unit cell, optimizing all internal coordinates; we then apply a series of strains to this optimized hexagonal unit cell. Two different strain types are applied: ε_1 and ε_{3+4} (see ESI†). For each strain, five different amplitudes of deformation are used: 0%, $\pm 0.5\%$, and $\pm 1\%$. Second, we relax atoms while fixing the deformed lattice parameters. By doing so, we obtain stress tensors σ_{ij} for all applied strains ε_{ij} . Third, C_{ij} are obtained from linear least squares fitting using the stress-strain relationship (the computed C_{ij} are given in the ESI†). Then, we calculate the single crystal elastic compliant constant S_{ij} as:

$$S_{ij} = C_{ij}^{-1}. \quad (3)$$

After obtaining C_{ij} and S_{ij} , the orientationally-averaged elastic moduli including Young's modulus E , bulk modulus B , shear modulus G , and Poissons ratio ν can be simply estimated

using the Voigt-Reuss-Hill (VRH) average.⁶⁴ The detailed formulae used for all reported quantities in this work are given in the ESI†.

3 Results and discussion

3.1 CO₂ binding energies

Fig. 1a depicts the optimized crystal structure of mmen-Zn₂(dobpdc), which consists of a periodic arrangement of ZnO₅ square pyramidal units, dobpd⁴⁻ linkers, and mmen ligands crystallizing in the $P3_21$ space group. A right panel of Fig. 1a shows that dangling amines interact with neighbors in the *ab*-plane *via* dispersive interactions between methyl groups. These interactions are reflected in the experimentally-determined crystal structure of mmen-Zn₂(dobpdc).⁶⁰ Our calculated lattice parameters for mmen-M₂(dobpdc) (M = Mg, Mn, Fe, Co, Zn) are given in Table 1. We do not include results for mmen-Ni₂(dobpdc) because the CO₂ capture mechanism of this framework is still under investigation. We note that our computed lattice parameters are not in perfect agreement with

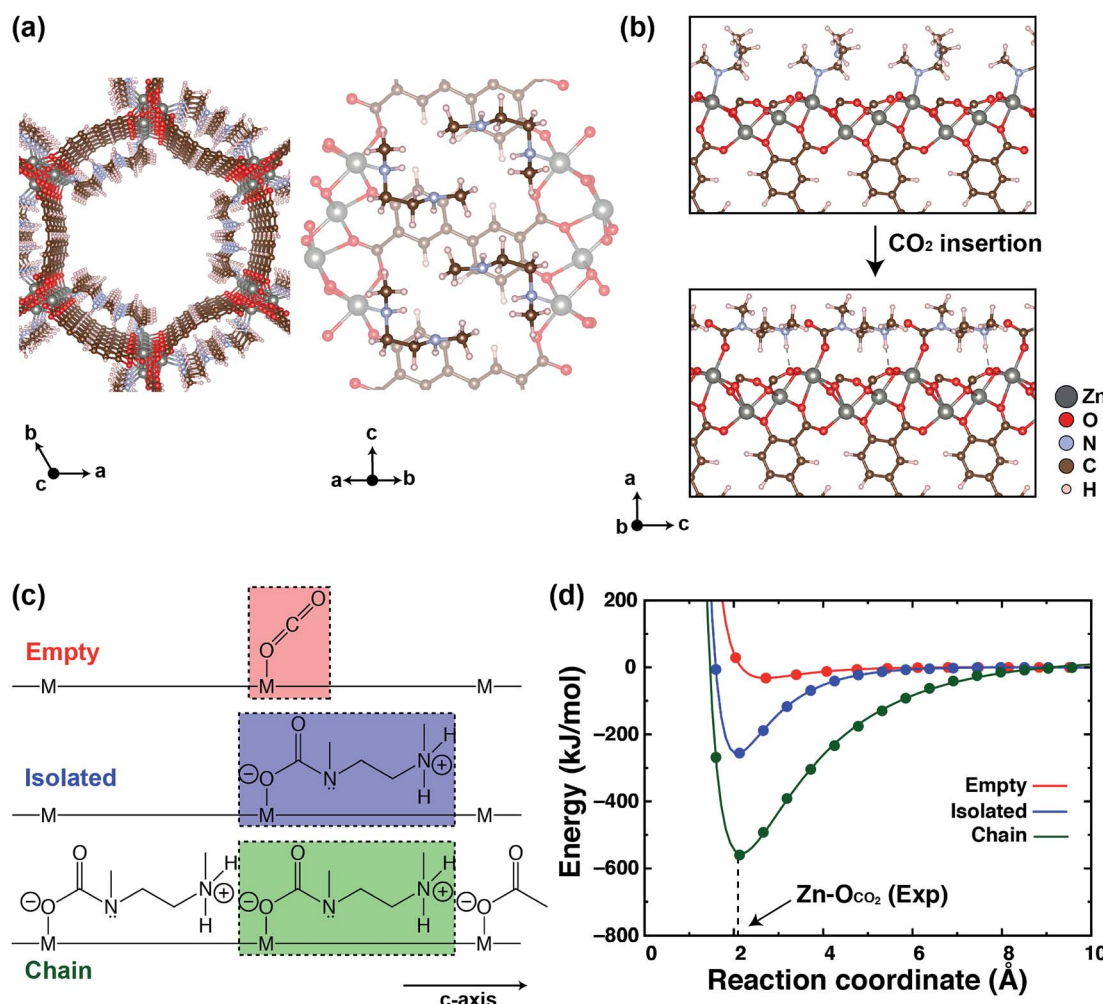


Fig. 1 (a) The optimized crystal structure of mmen-Zn₂(dobpdc). (b) Well-ordered ammonium carbamate chain formed upon CO₂ insertion. (c) Depictions of empty, isolated, and chain geometries along the channel direction (c-axis in the $P3_21$ setting). (d) Potential curves of empty, isolated, and chain geometries compared to the experimental Zn–O_{CO₂} distance indicated by the dotted line.

Table 1 Computed lattice parameters, M–N, and M–O distances for M_2 (dobpdc), mmen– M_2 (dobpdc), and CO_2 –mmen– M_2 (dobpdc) ($M = Mg, Mn, Fe, Co, Zn$) compared to experimental values (unit: Å).^{37,51,60} All structures are characterized in the space group $P3_221$

M	This work			Experiment		
	Empty	mmen–M	CO_2 –mmen–M	Empty	mmen–M	CO_2 –mmen–M
Mg	<i>a</i>	22.041	21.074	21.498	21.446	—
	<i>c</i>	6.939	6.672	7.005	6.824	—
	Mg–N	—	2.421	—	—	—
	Mg–O	—	—	2.072	—	—
Mn	<i>a</i>	22.253	22.650	21.788	21.629	21.729
	<i>c</i>	7.162	6.536	7.072	6.958	7.128
	Mn–N	—	2.432	—	—	2.289
	Mn–O	—	—	2.194	—	—
Fe	<i>a</i>	22.230	21.387	21.890	21.848	—
	<i>c</i>	6.963	6.622	7.013	6.814	—
	Fe–N	—	2.408	—	—	—
	Fe–O	—	—	2.195	—	—
Co	<i>a</i>	22.086	21.263	21.639	21.537	—
	<i>c</i>	6.920	6.540	7.005	6.798	—
	Co–N	—	2.324	—	—	—
	Co–O	—	—	2.147	—	—
Zn	<i>a</i>	22.087	21.683	21.881	21.547	21.391
	<i>c</i>	6.973	7.251	6.833	6.775	6.896
	Zn–N	—	2.212	—	—	2.155
	Zn–O	—	—	2.127	—	—

the experimental values, as expected. As the reparametrized PW86 exchange functional in the vdW-DF2 exchange–correlation functional overestimates repulsive interactions, equilibrium unit cell volumes, and bond distances,^{59,65,66} the computed lattice parameters and unit cell volumes of M_2 (dobpdc), CO_2 –mmen– M_2 (dobpdc), and CO_2 –mmen–Zn₂(dobpdc) are generally larger than the experimental values as shown in Table 1. In addition, our calculations with periodic boundary conditions do not capture any disorder associated with the mmen and CO_2 –mmen units shown in Fig. S3.† Any degree of disorder in these mmen and CO_2 –mmen units can alter the average structural properties including the lattice parameters, unit cell volumes, and bond lengths. As example of this, our DFT calculations show that a different mmen ordering of mmen–Fe₂(dobpdc) significantly changes the *a*- and *c*-axes – by about 0.7 Å and 0.4 Å, respectively – and the unit cell volume by 12.5% (see Fig. S4†). Moreover, according to the previous experimental study by some of us,⁶⁰ disordered solvent (toluene) is likely present in the pores of the single-crystal structure of mmen–Zn₂(dobpdc), for which structural data are collected using a solvated crystal; furthermore, the CO_2 -inserted single crystal structure of mmen–Zn₂(dobpdc) was refined to have 75% occupancy of ammonium carbamate chains, indicating the presence of solvent, CO_2 , or water at the remaining Zn(II) sites. Hence, these features are mainly responsible for the discrepancies. Nevertheless, despite the presence of some disorder, our vdW-corrected DFT calculations accurately predict the CO_2 binding energies (see Table 2) and give the powder diffraction patterns in good overall agreement with the experiments as shown in Fig. S5 and S6.†

Previous experimental^{32,37} and computational studies³⁸ demonstrated that mmen– M_2 (dobpdc) ($M = Mg, Mn, Fe, Co, Zn$) exhibit step-like isotherms above a threshold CO_2 partial

pressure, and that these steps originate from a mechanism wherein CO_2 gas molecules cooperatively and reversibly insert into metal–mmen bonds followed by formation of a well-ordered ammonium carbamate chain structure, as shown in Fig. 1b. Table 2 compares the computed CO_2 binding enthalpies (H_B) from this study with those obtained from experiment,³⁷ revealing that our vdW-DF2 calculations can accurately predict CO_2 binding enthalpies within ~5 kJ mol⁻¹. According to our calculations, in all cases MOFs with mmen exhibit an ~30 kJ mol⁻¹ enhancement in H_B compare to the unfunctionalized frameworks (see Tables 2 and 4).

To understand this increase, we performed calculations using three geometries as presented in Fig. 1c. We use the term “Empty” to indicate unappended M_2 (dobpdc) and “Chain” to indicate the structure with well-ordered ammonium carbamate chains along the channel direction (*c*-axis in the space group $P3_221$). The term “Isolated” refers to an alternative scenario in

Table 2 A comparison of computed CO_2 binding energies (E_B) and enthalpies (H_B) (in kJ mol⁻¹) in mmen– M_2 (dobpdc) ($M = Mg, Mn, Fe, Co, Zn$) with the experimental values at a CO_2 loading of 2 mmol g⁻¹.³⁷ Zero-point energy (ZPE) and thermal energy (TE) corrections of ammonium carbamate and mmen are considered. All ZPE and TE values are computed at 298 K

	This work			Exp	
	E_B	ZPE	TE	H_B	H_B
Mg	74.7	-2.8	1.1	73.0	71
Mn	68.9	-2.2	0.6	67.3	67
Fe	56.2	-1.9	0.7	55.1	58
Co	52.4	-1.3	0.4	51.6	52
Zn	62.4	-1.5	1.3	62.1	57



which there is no chain formation, and the calculations consider an ammonium carbamate unit bound at just one of the metal sites in the unit cell, with the other metal sites empty.

We then compute the potential interatomic distance curves for the three geometries, varying the separation between CO_2 and its binding site, by adopting a $a \times b \times 2c$ supercell for the isolated and chain geometries. Fig. 1d shows the calculated energy as a function of $\text{Zn}-\text{O}_{\text{CO}_2}$ distance, relative to the experimental $\text{Zn}-\text{O}_{\text{CO}_2}$ distance of 2.087(4) Å for the chain geometry. Similar curves are given for $\text{M} = \text{Mg, Mn, Fe, Co}$ in Fig. S7 in the ESI.† To calculate these curves, we systematically displace a CO_2 molecule and ammonium carbamate along the direction of the ground state $\text{Zn}-\text{O}$ bond to CO_2 .

In our DFT calculations, the vdW-DF2 functional slightly overestimates (by ~2%) the $\text{Zn}-\text{O}$ distance (2.127 Å) compared with experiment (2.087(4) Å), as reported in previous DFT studies.^{39,66} In Fig. 1d, the isolated and chain geometries have much deeper binding curves with higher curvature when compared to the empty geometry, reflecting the fact that the binding strength of ammonium carbamate to the MOF interior is much stronger than that of CO_2 alone. The binding enthalpy of CO_2 in the empty geometry is 29.3 kJ mol⁻¹, which is comparable to the values computed and experimentally measured for $\text{Zn}_2(\text{dobdc})$ (30.2 kJ mol⁻¹ and 26.8 ± 0.1 kJ mol⁻¹, respectively).^{28,29} On the other hand, the binding enthalpy of an ammonium carbamate (H_{iso}) in the isolated geometry is 259.0 kJ mol⁻¹, approximately nine times that of the CO_2 binding enthalpy. More interestingly, the ammonium carbamate binding enthalpy (H_{chain}) in the chain geometry is 562.1 kJ mol⁻¹, which is two times larger than that of the isolated geometry. The other MOFs also show similar behavior (see Fig. S7, ESI†). Thus the magnitude of the electrostatic interaction between two ammonium carbamate units in the chain geometry is equal to 151.5 kJ mol⁻¹ ($= (H_{\text{chain}} - H_{\text{iso}})/2$) (because ammonium carbamate unit interacts with two neighboring CO_2 -mmen sites along the pore axis, we divide by two). This large interaction energy is dominated by the ion pairing and hydrogen bonding interactions of the ammonium group to the unbound oxygen atom of the neighboring carbamate. In magnitude, these interactions are comparable to the heat of formation for ammonium carbamate (~152 kJ mol⁻¹).⁶⁷ The results of these calculations show that cooperative CO_2 insertion is a very favorable spontaneous process, that the carbamate chain geometry is quite stable, and that electrostatic interactions play a key role in the stability of CO_2 -mmen- $\text{M}_2(\text{dobpdc})$ (chain geometry).

The apparent enhancement of CO_2 binding strength by the presence of mmen can be qualitatively understood by considering how charges rearrange at the metal sites upon CO_2 binding. Fig. 2 shows the charge density difference ($\Delta\rho = \rho_{\text{MOF+molecule}} - (\rho_{\text{MOF}} + \rho_{\text{molecule}})$) isosurface plots for CO_2 -mmen binding sites in the isolated and chain geometries. The $\Delta\rho$ value calculated for the empty geometry is negligible compared to the values of the isolated and chain geometries at the same isosurface level (see Fig. S8, ESI†). In the isolated geometry, two sites are visible with prominent charge redistribution. One is the $\text{Zn}-\text{O}$ (carbamate) bond formed upon CO_2

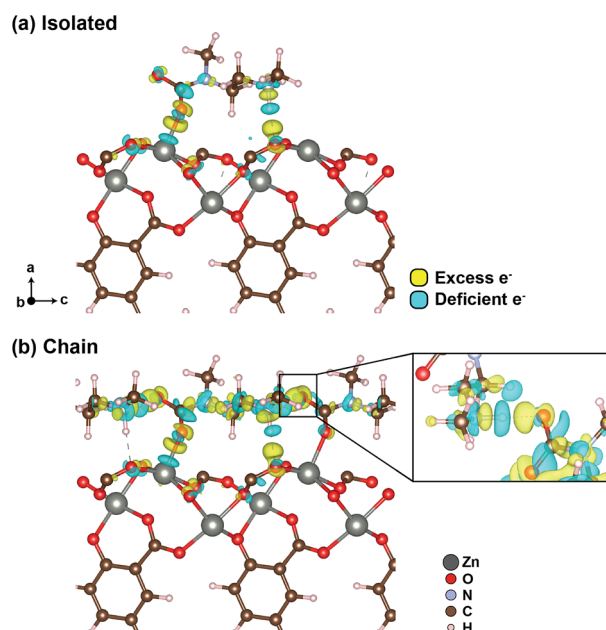


Fig. 2 Isosurface plots of the charge density difference ($\Delta\rho$) for the CO_2 -mmen binding site in (a) isolated and (b) chain structures. The isosurface level is equal to $0.02 \text{ e } \text{\AA}^{-3}$.

insertion into the $\text{Zn}-\text{mmen}$ bond, and the other is $\text{N}-\text{H}\cdots\text{O}$, which corresponds to hydrogen bonding between the ammonium group of ammonium carbamate and the non-bridging carboxylate oxygen atom on the dobpd c^{4-} linker (Fig. 2a). More interestingly, in the case of the chain geometry there are two additional sites in which ammonium carbamate units interact with their neighbors along the channel direction, as shown in the inset of Fig. 2b. These additional attractive interactions deepen the potential curve compared to the isolated structure (Fig. 1d). Our calculations therefore suggest that strong electrostatic interactions between ammonium carbamate units primarily drive the cooperative CO_2 insertion in mmen- $\text{M}_2(\text{dobpdc})$ and significantly enhance the CO_2 binding strength over non-amine-functionalized MOFs.

3.2 Mechanical properties

Having quantified the CO_2 binding enhancement afforded by mmen, we now address the mechanical properties of empty and CO_2 -loaded MOFs, which can be calculated *via* the elastic modulus C and the curvature of the binding curves ($\frac{\partial^2 E_{\text{tot}}}{\partial r^2}$) in the linear elastic regime,^{68,69} where E_{tot} is the total energy and r is reaction coordinate. From the binding energy curves shown in Fig. 1d and S7,† we expect that elastic moduli of mmen- $\text{M}_2(\text{dobpdc})$ and CO_2 -mmen- $\text{M}_2(\text{dobpdc})$ will be much larger than that of $\text{M}_2(\text{dobpdc})$, and that CO_2 adsorption and functionalization can strongly and reversibly alter these quantities. This is because the elastic modulus C is directly proportional to the curvature of the binding curves ($C \sim \frac{\partial^2 E_{\text{tot}}}{\partial r^2}$). Our calculations of the Young's modulus E , bulk modulus B , shear



modulus G , and Poisson's ratio ν for M_2 (dobpdc), mmn-M₂-(dobpdc), and CO_2 -mmn-M₂(dobpdc) are summarized in ESI Section 5.† In Fig. 3, we illustrate three-dimensional contours of directionally-dependent values of E for all the frameworks considered. In general, mmn and ammonium carbamate units greatly enhance E along all directions. The most prominent enhancement occurs along the channel direction, along which the ammonium carbamate chains run.

We now examine more quantitatively the effect of mmn and ammonium carbamate units on E , B , G , and ν . The orientationally-averaged E , B , G , and ν values obtained from eqn (1)–(8) in the ESI† are summarized in Table 3. Averaged over all directions, these values can be considered as elastic moduli of polycrystalline samples with randomly-oriented grains of equal volume fraction. As shown in Fig. 4, E , B , and G are generally larger for mmn-M₂(dobpdc) and CO_2 -mmn-M₂(dobpdc) than for M_2 (dobpdc), an enhancement that can be attributed to mmn and ammonium carbamate units, and this is most pronounced for E and G . For example, the magnitude of E for mmn-Zn₂(dobpdc) increases by 112% compared to that of Zn₂(dobpdc). More remarkably, the magnitude of E for CO_2 -mmn-Mn₂(dobpdc) increases by 141% compared to that of Mn₂(dobpdc) (see Table 3). All E values for mmn-M₂(dobpdc) and CO_2 -mmn-M₂(dobpdc) (10.7–16.7 GPa) are higher than the experimental values of conventional frameworks such as MOF-5 (2–8 GPa), HKUST-1 (6 GPa), and ZIFs (2–9 GPa), and lower than that of the hybrid MOF MOFP-1 (23–27 GPa).^{70–72} For G , the enhancement is even larger than that of E , for instance the G values of mmn-Zn₂(dobpdc) and CO_2 -mmn-Mn₂(dobpdc) increase by 124% and 159% compared to Zn₂(dobpdc) and Mn₂(dobpdc). All G values (4.0–6.4 GPa) are comparable to those of Zr-Uo-67 (5.69 GPa) and Zr-Uo-68 (4.18 GPa).⁷³

Our calculations thus show that mmn and CO_2 binding play a key role in the enhancement of the mechanical properties of the M_2 (dobpdc) framework materials. Moreover, these results demonstrate that the mechanical properties of MOFs can be tuned by functionalization with ligands such as mmn.

Table 3 Computed orientationally-averaged Young's modulus E (in GPa), bulk modulus B (in GPa), shear modulus G (in GPa), Poisson's ratio ν , and enhancement of E and G for M_2 (dobpdc), mmn-M₂-(dobpdc), and CO_2 -mmn-M₂(dobpdc)

	E	B	G	ν	Enhancement	
					E	G
Mg	8.97	10.05	3.32	0.35		
mmn-Mg	14.10	10.49	5.53	0.28	57%	67%
CO_2 -mmn-Mg	16.66	14.52	6.37	0.31	86%	92%
Mn	6.42	11.98	2.28	0.41		
mmn-Mn	10.72	10.36	4.04	0.33	67%	77%
CO_2 -mmn-Mn	15.48	13.66	5.90	0.31	141%	159%
Fe	8.63	9.69	3.19	0.35		
mmn-Fe	13.56	9.55	5.37	0.26	57%	68%
CO_2 -mmn-Fe	13.64	14.22	5.09	0.34	58%	59%
Co	6.95	8.51	2.55	0.36		
mmn-Co	10.66	8.24	4.15	0.28	53%	63%
CO_2 -mmn-Co	15.05	13.51	5.73	0.31	117%	125%
Zn	6.89	10.28	2.48	0.39		
mmn-Zn	14.58	13.03	5.55	0.31	112%	124%
CO_2 -mmn-Zn	14.02	15.28	5.21	0.35	103%	110%

Importantly, this bears direct relevance to CO_2 capture applications, since carbon capture materials must be mechanically robust and should not exhibit mechanical fatigue during CO_2 uptake and release cycling. Relatedly, it has been shown that functionalization with ligands such as mmn can significantly reduce plasticization and enhance selectivity in membrane-type devices.^{74–76}

3.3 CO_2 selectivity

In previous multicomponent adsorption measurements incorporating humidity,³² mmn-Mg₂(dobpdc) and mmn-Ni₂-(dobpdc) maintained high CO_2 selectivity, while Mg₂(dobpdc) and Ni₂(dobpdc) exhibited poor CO_2 capture performance under humid conditions. Mason *et al.* demonstrated that H_2O does not alter the cooperative CO_2 capture mechanism in mmn-

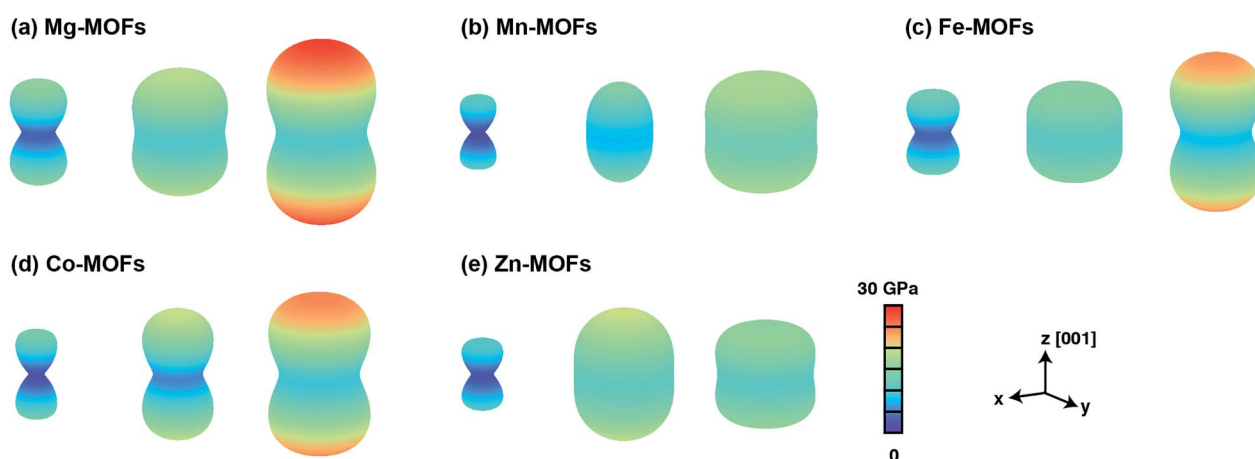


Fig. 3 Three-dimensional contour of directionally-dependent Young's moduli E for (a) Mg-MOFs, (b) Mn-MOFs, (c) Fe-MOFs, (d) Co-MOFs, and (e) Zn-MOFs. Left, center, and right panels correspond to M_2 (dobpdc), mmn-M₂(dobpdc), and CO_2 -mmn-M₂(dobpdc), respectively. The z -axis or [001] direction is the channel direction.



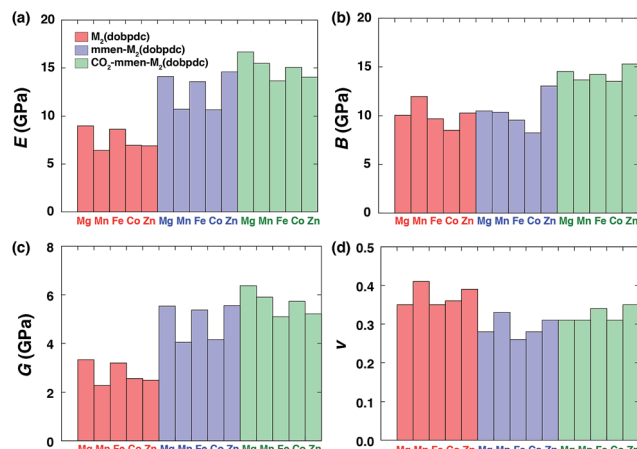


Fig. 4 The computed orientationally-averaged (a) Young's modulus E , (b) bulk modulus B , (c) shear modulus G , and (d) Poisson's ratio v values for all frameworks under consideration.

$Mg_2(\text{dobpdc})$,³² showing that instead $\text{mmnen-}Mg_2(\text{dobpdc})$ maintains a significant CO_2 capacity under multicomponent equilibrium conditions. However, the structural and energetic influence of H_2O on CO_2 adsorption in $\text{mmnen-}M_2(\text{dobpdc})$ remains unknown.

To address this question, we computed H_B for CO_2 , H_2O , and N_2 in the $M_2(\text{dobpdc})$ and $\text{mmnen-}M_2(\text{dobpdc})$ frameworks. Table 4 shows the computed enthalpies of first and second guest molecules (CO_2 , H_2O , and N_2) in the frameworks with and without mmnen functionalization. In the bare frameworks, water has the highest H_B among all three guest molecules at open metal sites. Furthermore, H_2O also has the highest H_B at secondary binding sites when it has occupied the open metal sites.

Fig. 5a shows the most stable computed configuration of $Zn_2(\text{dobpdc})$ in the presence of H_2O without mmnen . Here, the secondary H_2O interacts with the first Zn -bound H_2O *via* hydrogen bonding. Previous multicomponent measurements^{32,77} on the smaller pore MOFs $Mg_2(\text{dobdc})$, $Co_2(\text{dobdc})$, and $Ni_2(\text{dobdc})$ are consistent with this configuration. In ref. 32, in the case of $Mg_2(\text{dobdc})$, the amount of CO_2 adsorbed was 0.5 mmol g^{-1} , while adsorbed H_2O reached over 15 mmol g^{-1} ($1.8 \text{ mmol H}_2\text{O}$ per mmol Mg). Moreover, the amount of CO_2 adsorbed in $Ni_2(\text{dobdc})$ is almost zero while that of H_2O is over 20 mmol g^{-1} ($3.1 \text{ mmol H}_2\text{O}$ per mmol Ni). Therefore, water molecules significantly degrade CO_2 selectivity in $M_2(\text{dobdc})$ frameworks, and our calculations show that the larger-pore $M_2(\text{dobpdc})$ frameworks will exhibit the same behavior (see Table 4).

In contrast, our calculations indicate that CO_2 insertion to form an O-bound carbamate for $\text{mmnen-}M_2(\text{dobpdc})$ frameworks is much more favorable than binding H_2O at the open metal site of the corresponding bare $M_2(\text{dobpdc})$ frameworks. As shown in Table 4, the ammonium carbamate binding enthalpies, H_{chain} including ZPE and TE corrections, are about ten times higher than those for H_2O for all $M_2(\text{dobpdc})$ frameworks. Thus, the $\text{mmnen-}M_2(\text{dobpdc})$ frameworks are predicted

Table 4 Computed binding enthalpies H_B (kJ mol^{-1}) of first (CO_2 , H_2O , N_2 , and $\text{CO}_2\text{-mmnen}$) and second guest molecules (CO_2 , H_2O , and N_2) in $M_2(\text{dobpdc})$ and $\text{mmnen-}M_2(\text{dobpdc})$ ($M = \text{Mg, Mn, Fe, Co, Zn}$)

	First guest	H_B	Second guest	H_B
Mg	H_2O	62.6	H_2O	39.4
	CO_2	38.5	CO_2	25.3
	N_2	27.3	N_2	16.0
	CO_2	34.7	H_2O	40.9
	N_2	23.6	CO_2	26.3
	$\text{CO}_2\text{-mmnen-Mg}$	597.0	N_2	11.2
Mn	H_2O	54.6	H_2O	42.9
	CO_2	34.7	CO_2	26.6
	N_2	23.6	N_2	18.0
	CO_2	34.7	H_2O	43.3
	N_2	23.6	CO_2	29.4
	$\text{CO}_2\text{-mmnen-Mn}$	582.2	N_2	14.6
Fe	H_2O	53.9	H_2O	42.8
	CO_2	35.6	CO_2	20.3
	N_2	24.6	N_2	11.5
	CO_2	35.6	H_2O	40.1
	N_2	24.6	CO_2	25.3
	$\text{CO}_2\text{-mmnen-Fe}$	588.4	N_2	9.5
Co	H_2O	53.0	H_2O	38.7
	CO_2	34.9	CO_2	23.8
	N_2	22.4	N_2	10.9
	CO_2	34.9	H_2O	39.5
	N_2	22.4	CO_2	25.7
	$\text{CO}_2\text{-mmnen-Co}$	570.3	N_2	10.6
Zn	H_2O	44.2	H_2O	38.6
	CO_2	29.3	CO_2	23.2
	N_2	18.6	N_2	16.7
	CO_2	29.3	H_2O	40.5
	N_2	18.6	CO_2	23.7
	$\text{CO}_2\text{-mmnen-Zn}$	562.1	N_2	8.2

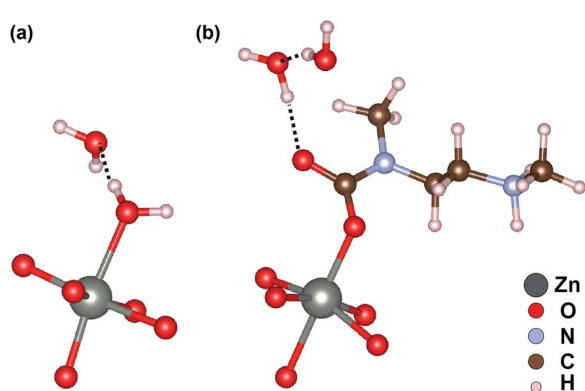


Fig. 5 The most stable configurations of (a) $Zn_2(\text{dobpdc})$ and (b) $\text{mmnen-}Zn_2(\text{dobpdc})$ in the presence of a mixture of CO_2 , H_2O , and N_2 .

to maintain their unique CO_2 capture mechanism even under humid conditions. Interestingly, our energetics suggest that H_2O molecules bind near the negatively charged end of the carbamate *via* hydrogen bonding interactions (Fig. 5b). This configuration also explains the large amount of H_2O adsorbed from the mixture of CO_2 , H_2O , and N_2 in CO_2 -mmen- Mg_2 - (dobpdc) .³² In previous multicomponent measurements with mmen- Mg_2 (dobpdc), the amount of H_2O adsorbed from the mixture was about 7 mmol g⁻¹ (1.7 H_2O per mmen- Mg), while CO_2 adsorbed from the mixture was about 4.2 mmol g⁻¹ (1.0 CO_2 per mmen- Mg). In fact, we find that accumulated H_2O increases the $\text{CO}_2 H_B$ by an amount equal to the H_2O binding strength. For example for mmen- Mn_2 (dobpdc), the binding energy of the second adsorbed H_2O molecule hydrogen-bonded to non-bonded O ion on the carbamate *via* hydrogen bonding (Fig. 5b) is as high as 43.3 kJ mol⁻¹. Thus, the additional hydrogen bonding in the presence of H_2O can further stabilize the $\text{CO}_2 H_B$ by the same amount (=43.3 kJ mol⁻¹). We speculate that this may be related to an increase of the amount of CO_2 adsorbed in the presence of H_2O .³² As a result, our computed energetics demonstrate that instead of hampering the CO_2 capture process, H_2O plays a crucial role in affording stability to CO_2 -mmen- M_2 (dobpdc).

4 Conclusions

We have examined the effect of mmen on the binding enthalpies and mechanical properties of mmen- M_2 (dobpdc) ($\text{M} = \text{Mg, Mn, Fe, Co, Zn}$), finding that mmen ligands enhance the $\text{CO}_2 H_B$ and selectivity under humid conditions, and that mmen and CO_2 -mmen ligands significantly enhance framework mechanical properties. These results elucidate the energetics of individual interactions underlying the cooperative CO_2 insertion mechanism in mmen- M_2 (dobpdc) under dry and humid conditions. Furthermore, our results demonstrate the remarkable increase in mechanical properties afforded by functionalization of M_2 (dobpdc) with diamines. Overall, our work highlights the unique advantages in CO_2 capture performance and physical properties accessible with diamine-appended frameworks.

Conflicts of interest

There are no conflicts to declare.

Acknowledgements

This work was supported by the Center for Gas Separations Relevant to Clean Energy Technologies, an Energy Frontier Research Center, funded by the U.S. Department of Energy, Office of Science, Office of Basic Energy Sciences, under Award DE-SC0001015. Work at the Molecular Foundry was supported by the Office of Science, Office of Basic Energy Sciences, U.S. Department of Energy, under Contract DE-AC02-05CH11231, and computational resources were provided by DOE (LBNL Lawrence and NERSC).

Notes and references

- 1 A. K. Cheetham, G. Férey and L. Thierry, *Angew. Chem., Int. Ed.*, 1999, **38**, 3268–3292.
- 2 S. L. James, *Chem. Soc. Rev.*, 2003, **32**, 276–288.
- 3 H. C. Zhou, J. R. Long and O. M. Yaghi, *Chem. Rev.*, 2012, **112**, 673–674.
- 4 J. L. C. Rowsell and O. M. Yaghi, *Microporous Mesoporous Mater.*, 2004, **73**, 3–14.
- 5 H. Furukawa, K. Cordova, M. O'Keeffe and O. M. Yaghi, *Science*, 2013, **341**, 1230444.
- 6 M. L. Foo, R. Matsuda and S. Kitagawa, *Chem. Mater.*, 2014, **26**, 310–322.
- 7 G. Férey, *Dalton Trans.*, 2009, 4400–4415.
- 8 O. K. Farha and J. T. Hupp, *Acc. Chem. Res.*, 2010, **43**, 1166–1175.
- 9 K. K. Tanabe and S. M. Cohen, *Chem. Soc. Rev.*, 2011, **40**, 498–519.
- 10 J. R. Long and O. M. Yaghi, *Chem. Soc. Rev.*, 2009, **38**, 1213–1214.
- 11 N. L. Rosi, J. Eckert, M. Eddaoudi, D. T. Vodak, J. Kim, M. O'Keeffe and O. M. Yaghi, *Science*, 2003, **73**, 12–15.
- 12 A. R. Millward and O. M. Yaghi, *J. Am. Chem. Soc.*, 2005, **127**, 17998–17999.
- 13 K. Sumida, D. L. Rogow, J. A. Mason, T. M. McDonald, E. D. Bloch, Z. R. Herm, T.-H. Bae and J. R. Long, *Chem. Rev.*, 2012, **112**, 724–781.
- 14 J. Liu, P. K. Thallapally, B. P. McGrail, D. R. Brown and J. Liu, *Chem. Soc. Rev.*, 2012, **41**, 2308–2322.
- 15 T. A. Makal, J.-R. Li, W. Lu and H.-C. Zhou, *Chem. Soc. Rev.*, 2012, **41**, 7761–7779.
- 16 International Energy Agency, *CO₂ Emissions From Fuel Combustion Highlights*, 2015.
- 17 F. Joos, G.-K. Plattner, T. F. Stocker, O. Marchal and A. Schmittner, *Science*, 1999, **284**, 464–467.
- 18 P. M. Cox, R. A. Betts, C. D. Jones, S. A. Spall and J. Totterdell, *Nature*, 2000, **408**, 184–187.
- 19 W. Zhou, H. Wu and T. Yildirim, *J. Am. Chem. Soc.*, 2008, **2**, 15268–15269.
- 20 S. R. Caskey, A. G. Wong-Foy and A. J. Matzger, *J. Am. Chem. Soc.*, 2008, **130**, 10870–10871.
- 21 E. D. Bloch, L. J. Murray, W. L. Queen, S. Chavan, S. N. Maximoff, J. P. Bigi, R. Krishna, V. K. Peterson, F. Grandjean, G. J. Long, B. Smit, S. Bordiga, C. M. Brown and J. R. Long, *J. Am. Chem. Soc.*, 2011, **133**, 14814–14822.
- 22 R. Sanz, F. Martínez, G. Orcajo, L. Wojtas and D. Briones, *Dalton Trans.*, 2013, **42**, 2392–2398.
- 23 W. L. Queen, C. M. Brown, D. K. Britt, P. Zajdel, M. R. Hudson and O. M. Yaghi, *J. Phys. Chem. C*, 2011, **115**, 24915–24919.
- 24 D. J. Xiao, E. D. Bloch, J. A. Mason, W. L. Queen, M. R. Hudson, N. Planas, J. Borycz, A. L. Dzubak, P. Verma, K. Lee, F. Bonino, V. Crocella, J. Yano, S. Bordiga, D. G. Truhlar, L. Gagliardi, C. M. Brown and J. R. Long, *Nat. Chem.*, 2014, **6**, 590–595.



25 P. D. C. Dietzel, Y. Morita, R. Blom and H. Fjellvåg, *Angew. Chem., Int. Ed.*, 2005, **44**, 6354–6358.

26 P. D. C. Dietzel, B. Panella, M. Hirscher, R. Blom and H. Fjellvåg, *Chem. Commun.*, 2006, **1**, 959–961.

27 Y. Liu, H. Kabbour, C. M. Brown, D. A. Neumann and C. C. Ahn, *Langmuir*, 2008, **24**, 4772–4777.

28 K. Lee, J. D. Howe, L.-C. Lin, B. Smit and J. B. Neaton, *Chem. Mater.*, 2015, **27**, 668–678.

29 W. L. Queen, M. R. Hudson, E. D. Bloch, J. A. Mason, M. I. Gonzalez, J. S. Lee, D. Gygi, J. D. Howe, K. Lee, T. A. Darwish, M. James, V. K. Peterson, S. J. Teat, B. Smit, J. B. Neaton, J. R. Long and C. M. Brown, *Chem. Sci.*, 2014, **5**, 4569–4581.

30 J. Yu and P. B. Balbuena, *J. Phys. Chem. C*, 2013, **117**, 3383–3388.

31 K. Tan, S. Zuluaga, Q. Gong, Y. Gao, N. Nijem, J. Li, T. Thonhauser and Y. J. Chabal, *Chem. Mater.*, 2015, **27**, 2203–2217.

32 J. A. Mason, T. M. McDonald, T.-H. Bae, J. E. Bachman, K. Sumida, J. J. Dutton, S. S. Kaye and J. R. Long, *J. Am. Chem. Soc.*, 2015, **137**, 4787–4803.

33 S. Zuluaga, E. M. A. Fuentes-Fernandez, K. Tan, F. Xu, J. Li, Y. J. Chabal and T. Thonhauser, *J. Mater. Chem. A*, 2016, **4**, 5176–5183.

34 J. Kundu, T. Pascal, D. Prendergast and S. Whitelam, *Phys. Chem. Chem. Phys.*, 2016, **18**, 21760–21766.

35 T. C. Drage, C. E. Snape, L. A. Stevens, J. Wood, J. Wang, A. I. Cooper, R. Dawson, X. Guo, C. Satterley and R. Irons, *J. Mater. Chem.*, 2012, **22**, 2815–2823.

36 T. M. McDonald, W. R. Lee, J. a. Mason, B. M. Wiers, C. S. Hong and J. R. Long, *J. Am. Chem. Soc.*, 2012, **134**, 7056–7065.

37 T. M. McDonald, J. A. Mason, X. Kong, E. D. Bloch, D. Gygi, A. Dani, V. Crocellà, F. Giordanino, S. O. Odoh, W. S. Drisdell, B. Vlaisavljevich, A. L. Dzubak, R. Poloni, S. K. Schnell, N. Planas, K. Lee, T. Pascal, L. F. Wan, D. Prendergast, J. B. Neaton, B. Smit, J. B. Kortright, L. Gagliardi, S. Bordiga, J. A. Reimer and J. R. Long, *Nature*, 2015, **519**, 303–308.

38 B. Vlaisavljevich, S. O. Odoh, S. K. Schnell, A. L. Dzubak, K. Lee, N. Planas, J. B. Neaton, L. Gagliardi and B. Smit, *Chem. Sci.*, 2015, **6**, 5177–5185.

39 R. Poloni, B. Smit and J. B. Neaton, *J. Phys. Chem. A*, 2012, **116**, 4957–4964.

40 P. Canepa, N. Nijem, Y. J. Chabal and T. Thonhauser, *Phys. Rev. Lett.*, 2013, **110**, 026102.

41 W. S. Drisdell, R. Poloni, T. M. McDonald, J. R. Long, B. Smit, J. B. Neaton, D. Prendergast and J. B. Kortright, *J. Am. Chem. Soc.*, 2013, **135**, 18183–18190.

42 B. Vlaisavljevich, J. Huck, Z. Hulvey, K. Lee, J. A. Mason, J. B. Neaton, J. R. Long, C. M. Brown, D. Alfé, A. Michaelides and B. Smit, *J. Phys. Chem. A*, 2017, **121**, 4139–4151.

43 T. Thonhauser, S. Zuluaga, C. A. Arter, K. Berland, E. Schröder and P. Hyldgaard, *Phys. Rev. Lett.*, 2015, **115**, 136402.

44 G. W. Mann, K. Lee, M. Cococcioni, B. Smit and J. B. Neaton, *J. Chem. Phys.*, 2016, **144**, 174104.

45 J.-C. Tan, B. Civalleri, C.-C. Lin, L. Valenzano, R. Galvelis, P.-F. Chen, T. D. Bennett, C. Mellot-Draznieks, C. M. Zicovich-Wilson and A. K. Cheetham, *Phys. Rev. Lett.*, 2012, **108**, 095502.

46 N. Planas, A. L. Dzubak, R. Poloni, L. C. Lin, A. McManus, T. M. McDonald, J. B. Neaton, J. R. Long, B. Smit and L. Gagliardi, *J. Am. Chem. Soc.*, 2013, **135**, 7402–7405.

47 W. S. Drisdell, R. Poloni, T. M. McDonald, T. A. Pascal, L. F. Wan, C. D. Pemmaraju, B. Vlaisavljevich, S. O. Odoh, J. B. Neaton, J. R. Long, D. Prendergast and J. B. Kortright, *Phys. Chem. Chem. Phys.*, 2015, **17**, 21448–21457.

48 S. A. Didas, M. A. Sakwa-novak, G. S. Foo, C. Sievers and C. W. Jones, *J. Phys. Chem. Lett.*, 2014, **5**, 4194–4200.

49 W. R. Lee, H. Jo, L.-M. Yang, H. Lee, D. W. Ryu, K. S. Lim, J. H. Song, D. Y. Min, S. S. Han, J. G. Seo, Y. K. Park, D. Moon and C. S. Hong, *Chem. Sci.*, 2015, **6**, 3697–3705.

50 L. A. Darunte, K. S. Walton, D. S. Sholl and C. W. Jones, *Curr. Opin. Chem. Eng.*, 2016, **12**, 82–90.

51 D. Gygi, E. D. Bloch, J. A. Mason, M. R. Hudson, M. I. Gonzalez, R. L. Siegelman, T. A. Darwish, W. L. Queen, C. M. Brown and J. R. Long, *Chem. Mater.*, 2016, **28**, 1128–1138.

52 J. P. Perdew, K. Burke and M. Ernzerhof, *Phys. Rev. Lett.*, 1996, **77**, 3865–3868.

53 P. E. Blöchl, *Phys. Rev. B: Condens. Matter Mater. Phys.*, 1994, **50**, 17953–17979.

54 G. Kresse and D. Joubert, *Phys. Rev. B: Condens. Matter Mater. Phys.*, 1999, **59**, 1758–1775.

55 G. Kresse and J. Hafner, *Phys. Rev. B: Condens. Matter Mater. Phys.*, 1993, **47**, 558–561.

56 G. Kresse and J. Furthmüller, *Phys. Rev. B: Condens. Matter Mater. Phys.*, 1996, **54**, 11169–11186.

57 G. Kresse and J. Furthmüller, *Comput. Mater. Sci.*, 1996, **6**, 15–50.

58 G. Kresse and J. Hafner, *Phys. Rev. B: Condens. Matter Mater. Phys.*, 1994, **49**, 14251–14269.

59 K. Lee, É. D. Murray, L. Kong, B. I. Lundqvist and D. C. Langreth, *Phys. Rev. B: Condens. Matter Mater. Phys.*, 2010, **82**, 081101.

60 R. L. Siegelman, T. M. McDonald, M. I. Gonzalez, J. D. Martell, P. J. Milner, J. A. Mason, A. H. Berger, A. S. Bhowm and J. R. Long, *J. Am. Chem. Soc.*, 2017, **139**, 10526–10538.

61 C. Elsässer, M. Fähnle, C. Chan and K. Ho, *Phys. Rev. B: Condens. Matter Mater. Phys.*, 1994, **49**, 13975–13978.

62 E. D. Bloch, W. L. Queen, R. Krishna, J. M. Zubairy, C. M. Brown and J. R. Long, *Science*, 2012, **335**, 1606–1611.

63 Y. Le Page and P. Saxe, *Phys. Rev. B: Condens. Matter Mater. Phys.*, 2002, **65**, 104104.

64 R. Hill, *Proc. Phys. Soc., London, Sect. A*, 1952, **65**, 349–354.

65 É. D. Murray, K. Lee and D. C. Langreth, *J. Chem. Theory Comput.*, 2009, **5**, 2754–2762.

66 I. Hamada, *Phys. Rev. B: Condens. Matter Mater. Phys.*, 2014, **89**, 121103.



67 K. G. Clark and H. C. Hetherington, *J. Am. Chem. Soc.*, 1927, **49**, 1909–1915.

68 D. A. Padmavathi, *Mater. Sci. Appl.*, 2011, **22**, 97–104.

69 *Handbook of Advanced Ceramics*, ed. S. Somiya, Academic Press, 2013.

70 J. C. Tan, T. D. Bennett and A. K. Cheetham, *Proc. Natl. Acad. Sci. U. S. A.*, 2010, **107**, 9938–9943.

71 J. C. Tan and A. K. Cheetham, *Chem. Soc. Rev.*, 2011, **40**, 1059–1080.

72 W. Li, A. Thirumurugan, P. T. Barton, Z. Lin, S. Henke, H. H. M. Yeung, M. T. Wharmby, E. G. Bithell, C. J. Howard and A. K. Cheetham, *Phys. Rev. B: Condens. Matter Mater. Phys.*, 2014, **136**, 7801–7804.

73 H. Wu, T. Yildirim and W. Zhou, *J. Phys. Chem. Lett.*, 2013, **4**, 925–930.

74 J. E. Bachman, Z. P. Smith, T. Li, T. Xu and J. R. Long, *Nat. Mater.*, 2016, **15**, 845–851.

75 J. E. Bachman and J. R. Long, *Energy Environ. Sci.*, 2016, **9**, 2031–2036.

76 L. Maserati, S. M. Meckler, J. E. Bachman, J. R. Long and B. A. Helms, *Nano Lett.*, 2017, **17**, 6828–6832.

77 R. Mercado, B. Vlaisavljevich, L.-C. Lin, K. Lee, Y. Lee, J. A. Mason, D. J. Xiao, M. I. Gonzalez, M. T. Kapelewski, J. B. Neaton and B. Smit, *J. Phys. Chem. C*, 2016, **120**, 12590–12604.

